NAVAL POSTGRADUATE SCHOOL

MONTEREY, CALIFORNIA

THESIS

PERFORMANCE OF THE SELF REFERENCING INTERFEROMETER IN THE PRESENCE OF SIMULATED DEEP TURBULENCE AND NOISE EFFECTS

by

Lee T. Johnson

December 2013

Thesis Co-Advisors: Brij N. Agrawal
Jae-Jun Kim

THIS PAGE INTENTIONALLY LEFT BLANK

REPORT DOCUMENTATION PAGE			Form Approved OMB No. 0704-0188
Public reporting burden for this collection of information is estimated to average 1 hour per response, including the time for reviewing instruction, searching existing data sources, gathering and maintaining the data needed, and completing and reviewing the collection of information. Send comments regarding this burden estimate or any other aspect of this collection of information, including suggestions for reducing this burden, to Washington headquarters Services, Directorate for Information Operations and Reports, 1215 Jefferson Davis Highway, Suite 1204, Arlington, VA 22202-4302, and to the Office of Management and Budget, Paperwork Reduction Project (0704-0188) Washington DC 20503.			
1. AGENCY USE ONLY *(Leave blank)*	**2. REPORT DATE** December 2013	**3. REPORT TYPE AND DATES COVERED** Master's Thesis	
4. TITLE AND SUBTITLE PERFORMANCE OF THE SELF REFERENCING INTERFEROMETER IN THE PRESENCE OF SIMULATED DEEP TURBULENCE AND NOISE EFFECTS		**5. FUNDING NUMBERS**	
6. AUTHOR(S) Lee T. Johnson			
7. PERFORMING ORGANIZATION NAME(S) AND ADDRESS(ES) Naval Postgraduate School Monterey, CA 93943-5000		**8. PERFORMING ORGANIZATION REPORT NUMBER**	
9. SPONSORING /MONITORING AGENCY NAME(S) AND ADDRESS(ES) N/A		**10. SPONSORING/MONITORING AGENCY REPORT NUMBER**	
11. SUPPLEMENTARY NOTES The views expressed in this thesis are those of the author and do not reflect the official policy or position of the Department of Defense or the U.S. government. IRB protocol number ____N/A____.			
12a. DISTRIBUTION / AVAILABILITY STATEMENT Approved for public release; distribution is unlimited		**12b. DISTRIBUTION CODE** A	

13. ABSTRACT (maximum 200 words)

Current laser weapon systems are limited to close range encounters because the laser beam attenuates quickly within the atmosphere. A phenomenon known as deep turbulence is characterized by strong scintillation and branch points in the wave-front phase. Many wave-front sensors perform poorly in the presence of deep turbulence, and are unable to accurately reconstruct the wave-front. This paper examines a wave-front sensor, the self-referencing interferometer (SRI) that is theoretically immune to the effects of deep turbulence.

The SRI is both simulated mathematically and constructed in the lab for comparison between analytical and experimental results. Performance of the SRI is analyzed in the presence of realistic deep turbulence effects generated by a spatial light modulator, and realistic noise effects introduced by the digital imaging system. Simulated results show a significant loss of signal level as turbulence is increased, but a resilience of the wave-front sensor above a signal-to-noise ratio of two. Analogously, in the experimental results the signal drops off rapidly with increasing levels of turbulence, and reaches unacceptably low levels above a Rytov number of 0.4. A qualitative analysis of the wave-front reconstruction shows remarkable similarity between simulated and experimental results, though the experimental results contain far more error induced branch points than in the simulation. Methods are being explored to boost the signal and reduce the noise at the camera to allow the system to handle higher levels of turbulence.

14. SUBJECT TERMS Adaptive optics, self-referencing interferometer, spatial light modulator, deep turbulence			**15. NUMBER OF PAGES** 67
			16. PRICE CODE
17. SECURITY CLASSIFICATION OF REPORT Unclassified	**18. SECURITY CLASSIFICATION OF THIS PAGE** Unclassified	**19. SECURITY CLASSIFICATION OF ABSTRACT** Unclassified	**20. LIMITATION OF ABSTRACT** UU

NSN 7540-01-280-5500 Standard Form 298 (Rev. 2-89)
Prescribed by ANSI Std. 239-18

THIS PAGE INTENTIONALLY LEFT BLANK

Approved for public release; distribution is unlimited

PERFORMANCE OF THE SELF REFERENCING INTERFEROMETER IN THE PRESENCE OF SIMULATED DEEP TURBULENCE AND NOISE EFFECTS

Lee T Johnson
Lieutenant, United States Navy
B.S., North Carolina State University, 2009

Submitted in partial fulfillment of the
requirements for the degree of

MASTER OF SCIENCE IN ASTRONAUTICAL ENGINEERING

from the

NAVAL POSTGRADUATE SCHOOL
December 2013

Author: Lee T. Johnson

Approved by: Brij N. Agrawal
Thesis Co-Advisor

Jae-Jun Kim
Thesis Co-Advisor

Knox T. Millsaps
Chair, Department of Mechanical and Aerospace Engineering

THIS PAGE INTENTIONALLY LEFT BLANK

ABSTRACT

Current laser weapon systems are limited to close range encounters because the laser beam attenuates quickly within the atmosphere. A phenomenon known as deep turbulence is characterized by strong scintillation and branch points in the wave-front phase. Many wave-front sensors perform poorly in the presence of deep turbulence, and are unable to accurately reconstruct the wave-front. This paper examines a wave-front sensor, the self-referencing interferometer (SRI) that is theoretically immune to the effects of deep turbulence.

The SRI is both simulated mathematically and constructed in the lab for comparison between analytical and experimental results. Performance of the SRI is analyzed in the presence of realistic deep turbulence effects generated by a spatial light modulator, and realistic noise effects introduced by the digital imaging system. Simulated results show a significant loss of signal level as turbulence is increased, but a resilience of the wave-front sensor above a signal-to-noise ratio of two. Analogously, in the experimental results the signal drops off rapidly with increasing levels of turbulence, and reaches unacceptably low levels above a Rytov number of 0.4. A qualitative analysis of the wave-front reconstruction shows remarkable similarity between simulated and experimental results, though the experimental results contain far more error induced branch points than in the simulation. Methods are being explored to boost the signal and reduce the noise at the camera to allow the system to handle higher levels of turbulence.

THIS PAGE INTENTIONALLY LEFT BLANK

TABLE OF CONTENTS

LIST OF FIGURES

THIS PAGE INTENTIONALLY LEFT BLANK

LIST OF TABLES

THIS PAGE INTENTIONALLY LEFT BLANK

LIST OF ACRONYMS AND ABBREVIATIONS

ALTB	Airborne Laser Test Bed
ALL	Airborne Laser Laboratory
AOCoE	Adaptive Optics Center of Excellence
DM	deformable mirror
DoD	Department of Defense
FSM	fast steering mirror
HEL	high energy laser
LaWS	laser weapon system
NPS	Naval Postgraduate School
orig	original
PSF	point spread function
rec	reconstructed
SHWS	Shack-Hartmann wave-front sensor
SLM	spatial light modulator
SNR	signal-to-noise ratio
SRI	self-referencing interferometer

THIS PAGE INTENTIONALLY LEFT BLANK

ACKNOWLEDGMENTS

First, I'd like to acknowledge Dr. Bautista Fernandez for his steadfast commitment to this research, and for his expertise in optical alignment and data collection. Dr. Fernandez put in many weeks of effort into acquiring, installing, and aligning dozens of optical elements to create the self-referencing interferometer as it is today. His assistance was indispensable in the collection of all of the data used in this research. I also want to thank Dr. Brij Agrawal, Dr. Jae Jun Kim, and Dr. Ty Martinez for their continual support and encouragement as my advisors. I wish to thank all of the members of the SRDC for taking time to listen to my ideas, offer advice, and provide support, especially Travis Axtell. Finally, I want to acknowledge my wife, Julie, for her tireless support, and for graciously enduring so many hours of loneliness while I was away working on this daunting task. Thank you all.

THIS PAGE INTENTIONALLY LEFT BLANK

I. INTRODUCTION

A. BACKGROUND AND MOTIVATION

High energy laser (HEL) weapon systems have been a focus of research for over 25 years in the Department of Defense. Laser weapon systems have historically been researched by the Air Force as a solution for missile defense, and have been tested aboard aircraft. Though tested successfully to defend against missiles at short range in the early 1980s aboard the Airborne Laser Laboratory (ALL), the system was never introduced operationally. Many advances in the field of beam control and adaptive optics have generated interest in a longer-range laser weapon system to shoot down ballistic missiles in boost phase. The Airborne Laser Test Bed (ALTB) program was established in the mid-1990s to explore this possibility. That program was cancelled in 2011 after more than a decade of research and development, but no operational system is yet being fielded as a result of the effort [1], [2]. In recent years the U.S. Navy has been actively pursuing the development of laser weapon system for use on ships. There have been some successes in the Navy's laser weapon system (LaWS) research, and the system has been employed to disable some small unmanned aircraft and small boats. That system is now scheduled to be installed aboard a navy ship in 2014 for operational use as a technology demonstrator [3], [4]. New laser technologies are advancing, and will be considered for various military applications in the next decade. These new technologies include solid-state lasers, and free-electron lasers. New applications for HEL weapon systems may include air defense, ground and maritime offense, space control, and urban operations [5].

While there are differences in each of these laser applications and technologies, there are common elements. Military applications of lasers would benefit greatly from increased range and accuracy, whether the laser system is in the kilowatt or megawatt range. All laser beams suffer from atmospheric attenuation when propagating through the air. This attenuation is especially troublesome in the maritime environment because of increased particulates in the air and relatively horizontal path. While the particles within the air and air molecules themselves can absorb, reflect, scatter, and otherwise disperse the energy contained in the laser beam, the motion of the air and the thermal

gradients between air masses will also cause a beam to lose its coherence as it passes through this turbulent medium. This is caused by rapidly changing indices of refraction, and inhomogeneities in the small masses of air that the beam encounters along its path [6]. A defining characteristic of laser beams is their spatial coherence. Spatial coherence is characterized by a constant wave-front amplitude and phase profile, which allows a laser beam to maintain its small diameter over long distances. If a laser beam encounters a turbulent medium it will lose its coherence [7]. A loss of coherence in the beam will cause beam dispersion, and the energy contained in the beam will be spread out. The farther the beam travels through the turbulent medium, the more aberrated the beam will become. The turbulent effects will eventually produce scintillation in the beam, which is an amplitude fluctuation across the electromagnetic field. This scintillation causes rapid degeneration of the beam and very little energy makes it to the target. The field of adaptive optics is dedicated to the study of correcting aberrated wave-fronts.

Many developments have been made in correcting for weak turbulence. Astronomical seeing from ground based telescopes is now very near the diffraction limit due to the advancement of adaptive optics [8]. While these advances have greatly impacted the scientific community, there is still much to be done in the area of HEL weapon systems. Weapon systems that would often benefit from increased range and accuracy within the Earth's atmosphere have a much bigger challenge than the relatively short path lengths and weak turbulence encountered by ground-based skyward- looking telescopes. This research focuses on adaptive optics applications requiring long path lengths through a turbulent medium.

B. DEEP TURBULENCE

For the purposes of this paper, the term "deep turbulence" will be used to describe aberrations with significant scintillation and branch points in the wave-front. Adaptive optics is still advancing in the area of deep turbulence. Traditional wave-front sensors such as the lateral sheering interferometer and Shack-Hartmann wave-front sensor are highly sensitive to the presence of scintillation and branch points, but there are more

novel wave-front sensors that are naturally immune to the effects of scintillation and branch points [9]. One such sensor, the SRI, is the subject of this investigation.

1. Scintillation

Scintillation is the fluctuation in amplitude of an optical wave-front caused by propagation through long path lengths or strong turbulence (or both) within a turbulent medium. When scintillation is strong enough, there can be areas of very low to zero intensity (squared amplitude) in the wave-front that present challenges to wave-front reconstructors. Scintillation is caused by the constructive and destructive interference of individual rays of light from a point source as they pass through a medium with varying indices of refraction between individual pockets along the propagation path. These minor angular deflections of individual light rays worsen over long path lengths to produce significant aberrations in the wave-front.

2. Branch Points and Branch Cuts

When scintillation becomes severe, as is the case with deep turbulence, the amplitude function can drop low enough to create areas of zero intensity in the wave-front. These areas represent a discontinuity in the phase function of the reconstructed wave-front. The discontinuity is physically interpreted as a jump of 2π radians in the phase. These discontinuities are known as branch points, and are unavoidable with increasing levels of turbulence [10]. Branch points occur in oppositely signed pairs, and are connected by an arbitrarily positioned line called a branch cut. Branch points are generally linked by a trough of low intensity. This trough is the most natural place to position the branch cut. This 2π jump causes a major problem for many types of wave-front reconstructors, and continuous face-sheet deformable mirrors, which have unavoidable correction error in the vicinity of branch cuts. Beam correction is most important in areas of high intensity, and thus branch cuts are placed in areas of lowest intensity [10]. Traditional wave-front reconstructors, such as the least mean square error wave-front reconstructor, calculate the phase of a point of interest by summing the phase differences along all possible paths from a phase reference point to the point of interest, and then averaging the multiplicity of results to reduce the effects of noise. This method

works well unless a number of those paths cross a branch cut, and a 2π discontinuity skews the results of the averaging [11].

3. Rytov Number

The Rytov number is a single number that can be used to describe the severity of aberration experienced by a monochromatic beam as it propagates through a turbulent medium. This number is useful because it gives an idea of the characteristics of the wave-front one should expect. Generally a Rytov number around 0.25 marks the onset of strong scintillation, and the appearance of branch points in the wave-front [12]. For the purposes of this paper, aberrations with a Rytov number above 0.25 will be considered deep turbulence. Rytov number is a function of propagation path length (L), wavelength of light (λ), and the index of refraction structure constant $\left(C_n^2\right)$, which is a measure of the severity of turbulence in the medium. The Rytov number is expressed as a statistical variance defined as [13]

$$\sigma_R^2 = 1.23 C_n^2 \left(\frac{2\pi}{\lambda}\right)^{\frac{7}{6}} L^{\frac{11}{6}} \quad . \tag{1}$$

Propagation path length generally varies between 10s and 100s of kilometers. Severe turbulence generally has a C_n^2 value greater than $10^{-13} meters^{(-2/3)}$. If propagation path length is short enough this may not cause scintillation in the wave-front. As a corollary, even if C_n^2 is relatively low and propagation path is very long, scintillation may still appear. This is why Rytov has been selected as a measure of aberration rather than C_n^2 alone.

C. SELF-REFERENCING INTERFEROMETER

Classifying the nature of the aberration on an incoming wave-front involves a camera, which acts as the wave-front sensor, and a reconstructor, which interprets the data collected by the wave-front sensor to reconstruct the wave-front phase. This paper analyzes one particular kind of wave-front sensor called the self-referencing interferometer (SRI). The SRI is ideal for use with deep turbulence because it measures

the wave-front field directly, and therefore is unaffected by branch points and scintillation. The SRI accomplishes direct measurement of the phase in a unique way that does not require the use of a traditional reconstruction method such as a least mean square error reconstructor.

The self-referencing interferometer is composed of a series of optical elements that generate four phase-shifted signal beams that have each been interfered with an equally phase-shifted reference beam. These four individual beams are then collected with a digital imaging system. The reconstruction is then accomplished with a simple formula that depends only on the intensity profile of the light in each of the four beams. Equation 2 is used to calculate the phase at each point (i, j) in the wave-front using the four individual intensity frames. There are multiple methods for creating an SRI using more or less than four frames. This particular method is known as the 4-bucket method. The wave-front phase is calculated by [14]

$$\varphi(i, j) = \tan^{-1}\left[\frac{I_4(i, j) - I_2(i, j)}{I_1(i, j) - I_3(i, j)}\right] \tag{2}$$

Where I_1, I_2, I_3, and I_4 correspond to intensities with 0, $\pi/2$, π, and $3\pi/2$ phase shift, respectively. The phase output will be from $-\pi$ to π and will need to be unwrapped before using a continuous face-sheet DM [15].

D. THESIS OBJECTIVE

The objective of this research is to create and characterize a SRI at the Naval Postgraduate School for use in on-going adaptive optics and beam control research. The SRI will be simulated in the MATLAB software program, and constructed in the laboratory. The SRI will be used to reconstruct wave-fronts containing strong scintillation and branch points. The performance of the SRI will be analyzed, and its limitations probed. Specifically, the ability of the SRI to qualitatively reproduce wave-fronts and identify branch point locations will be assessed. The SRI will be tested at a variety of turbulence and noise levels to determine the limits of its operation. Finally, areas will be identified for the improvement of performance of the SRI.

THIS PAGE INTENTIONALLY LEFT BLANK

II. SIMULATION

A. SELF REFERENCING INTERFEROMETER SIMULATION

The self-referencing interferometer was simulated in MATLAB using some basic mathematical equations and raw data provided by WaveProp. WaveProp is MATLAB third party toolbox written by the Optical Sciences Company. It is used to accurately simulate the effects of atmospheric turbulence on passing optical wave-fronts. The purpose of the simulation is to establish a model against which the experimental set-up can be measured. The simulation uses many of the same processes developed for the analysis of experimental data, and addresses the reality gap by implementing realistic camera noise. The simulation provides a standard of performance that should be attainable in experimentation after refinement of optical alignment, removal of excess system noise, and optimization of data processing techniques. Error can enter into the reconstruction during data processing because of a phenomenon known as misregistration. This occurs when there is misalignment between the four frames when the wave-front phase is calculated. For the reconstruction to be accurate, each pixel of each frame must align with its counterpart in the adjacent frame, so that the phase at that location can be calculated from the correct pixels.

WaveProp is provided a C_n^2 value, propagation path length, and wavelength. It produces amplitude and phase data corresponding to a specific Rytov number. Four intensity profiles are then generated via a simple formula that simulates the interference and phase shifting of the given amplitude and phase data [16]. These frames can be calculated using the equations,

$$\begin{aligned} I_1 &= A + A\cos\varphi \\ I_2 &= A - A\sin\varphi \\ I_3 &= A - A\cos\varphi \\ I_4 &= A + A\sin\varphi \end{aligned} \quad . \tag{3}$$

Once the four frames have been generated the phase reconstruction can be completed using Equation 2.

B. CAMERA NOISE

The simulated camera noise is composed of several different types of noise. Dark current is simulated by adding a frame of uniform intensity that corresponds to an integration time and a fixed rate of accumulation of electrons based on sensor temperature. Dark current can be very small (on the order of 1 electron per second) for a good imaging system. Imaging systems with built in cooling can achieve 50° C below ambient combined with integration times in the microsecond range. Pixel non-uniformity is simulated by generating a frame of Gaussian distributed numbers with a standard deviation of some small percent, and a mean value of one. This frame is then used as a scaling factor to multiply by the image frame to simulate the variation in sensitivity from pixel to pixel. Both dark current noise and pixel non-uniformity have been fixed for this simulation, and will not vary with changing SNR. For this simulation a dark current value of 10 electrons per pixel per second was used at an integration time of $1x10^{-3}$ seconds, and the value for pixel non-uniformity was five percent standard deviation.

The system read noise, or on-chip noise, represents the noise introduced by the charge coupled device (CCD). This value can be very low for a low noise camera, on the order of 15 photo electrons RMS [17]. Read noise is given by the equation,

$$\sigma_{read}^2 = \left(LSB\right)^2 \tag{4}$$

The off-chip noise is introduced by the analog to digital converter (ADC), and corresponds to the error introduced in the conversion of photons to digital signal [18]. The variance in this noise is given by the equation,

$$\sigma_q^2 = \frac{1}{16}\left(LSB\right)^2 , \tag{5}$$

where LSB is the number of electrons per least significant bit of the 16-bit ADC.

Finally, the shot noise is a function of the random arrival time of photons within the imaged wave-front and is described by the equation,

$$\sigma_{shot}^2 = \frac{\eta_{qe}}{N_{split}}\left[\frac{I_s + I_r}{2}\right] , \tag{6}$$

where η_{qe} is the quantum efficiency of the camera, N_{split} is the number of interferograms (four in this case), and I_s and I_r are the average intensities of the signal and reference beams respectively [18]. In practice the signal and reference beams can be imaged separately by blocking one or the other beam to get an accurate value for the intensities. This value will obviously change depending on the level of turbulence [18]. The total system noise is then given by equation,

$$\sigma_{sys} = \sqrt{\sigma_{shot}^2 + \sigma_{read}^2 + \sigma_q^2} \tag{7}$$

This standard deviation of the total system noise can be used to generate a noise frame Gaussian noise frame is then added to the image frame. These three types of noise are used to realistically simulate the noise introduced by the imaging system, and can be individually tweaked to yield a signal to noise ratio (SNR) comparable to the experimental setup, or to test the performance under different noise conditions.

The SNR is defined as the mean signal strength (μ) divided by the standard deviation of the noise (σ_{sys}), and is given by the equation,

$$SNR = \frac{\mu}{\sigma_{sys}} \tag{8}$$

While this is obviously only an approximation of a much more complicated and dynamic effect, it can be used to measure the response of the SRI in low SNR environments. Shown in Figure 1 is a sample noise frame representative of noise that will be added to test the SRI's response to low SNR.

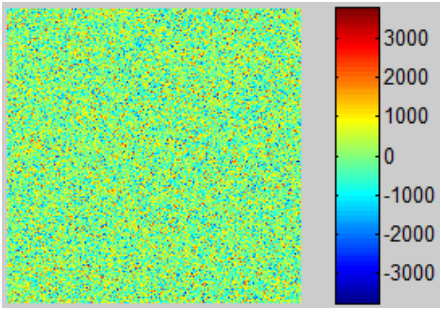

Figure 1. Sample noise frame used to test SRI resilience to Gaussian noise effects.

C. PERFORMANCE METRIC

The quality of the reconstruction is measured by the estimation Strehl ratio [18],

$$S = \frac{\left| \left[\sum_{i=1}^{N} \sum_{j=1}^{N} u_{orig}(i,j) u_{rec}^{*}(i,j) \right] \right|^2}{\left[\sum_{i=1}^{N} \sum_{j=1}^{N} \left| u_{orig}(i,j) \right| \right]^2} . \quad (9)$$

If the wave-front is reconstructed exactly as it was entered, the Strehl ratio will be one. With simulated noise effects added to the data, the Strehl ratio will be less than one. By testing a variety of cases, the performance of the SRI can be estimated in the presence of varying levels of turbulence and noise effects. The original wave-front (u_{orig}) that was generated by WaveProp is provided to the SRI simulation, and is used as a baseline against which the reconstructed wave-front (u_{rec}) is measured. The WaveProp amplitude and phase data are scaled to match the frame size of the experimental data at 200×200 pixels, and every pixel in that frame has its phase calculated within the SRI simulation to yield the reconstructed wave-front data.

The simulation was run for several values of Rytov numbers to observe the general trends of increasing both Rytov number and SNR as shown in Table 1.

Rytov Number	SNR	Strehl Ratio
0.301	4	0.950
0.301	2	0.827
0.301	1	0.539
2.092	4	0.943
2.092	2	0.822
2.092	1	0.570
3.313	4	0.942
3.313	2	0.822
3.313	1	0.568

Table 1. Strehl ratio shown for a variety of Rytov numbers and SNRs.

The trend here indicates that SRI performance is theoretically independent of turbulence level, but is more explicitly linked to SNR. It is true that in most cases increased levels of turbulence will in fact attenuate the signal and lead to lower SNR, but if signal level can be maintained despite high levels of turbulence, then the reconstruction retains fidelity. Also, it can be seen that for Gaussian noise only, the SNR cannot drop much below two for the reconstruction to remain valid.

THIS PAGE INTENTIONALLY LEFT BLANK

III. EXPERIMENTATION

A. EXPERIMENTAL SET-UP AND DATA COLLECTION

The SRI was built within the Adaptive Optics Center of Excellence (AOCoE) at the Naval Postgraduate School (NPS). The major components of the setup are the laser source, the spatial light modulator (SLM), the SRI, and the digital imaging system. The experimental setup begins at the source of the laser light. In this case the source is a 2.5 mW laser at 632 nm (red). The laser propagates from the source to the SLM where the wave-front is inflicted with a high degree of aberration to simulate the effects of deep turbulence. The reflected light from the SLM is polarized so that it follows a different return path than the incident light. The light is then propagated to the SRI where it is split into the four phase-shifted interfered beams used for wave-front reconstruction. These components are part of a more complex set-up at the Adaptive Optics Center of Excellence (AOCoE) at the Naval Postgraduate School (NPS), shown in Figure 2.

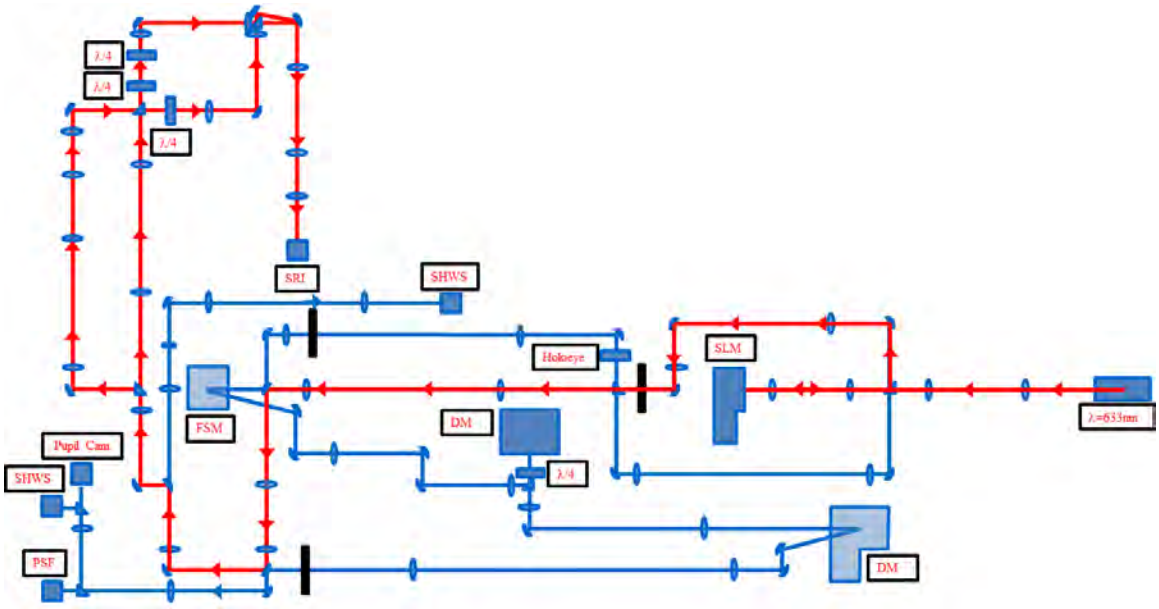

Figure 2. Adaptive optics test-bed at the Naval Postgraduate School. Optical path used in SRI experimentation is shown here in red.

Figure 3 is a photograph of the test-bed as it is today. This image was captured from the right side of the test-bed, with the laser source just off camera to the right.

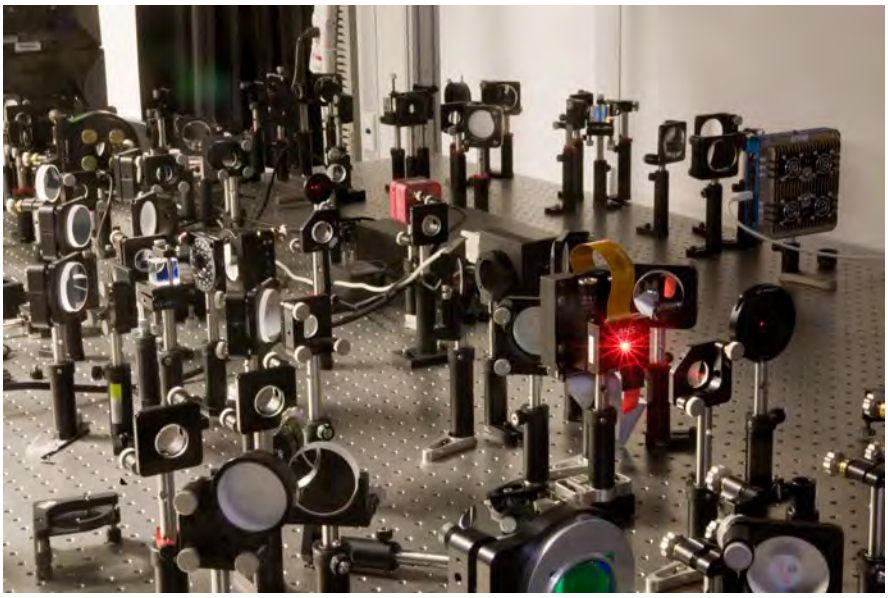

Figure 3. Adaptive optics test-bed at the Naval Postgraduate School.

Increasing the level of turbulence at the SLM causes the signal to attenuate proportionally, and thus there is a loss of intensity at the wave-front sensor as Rytov number increases. This loss of signal causes a decrease in signal-to-noise ratio, which negatively affects the overall fidelity of the reconstruction. The goal is to either reduce the noise enough, or increase the signal enough to avoid significant impact to the reconstruction process. The signal strength can be increased by replacing low quality optics with higher quality, more reflective optics or by increasing the integration time at the sensor. The noise can be reduced either by reducing the temperature of the sensor, filtering or blocking stray light, or by using more advanced techniques such as flat fielding or frame averaging to reduce the overall level of Gaussian random noise [19].

B. SPATIAL LIGHT MODULATOR

The SLM is a 512×512 liquid crystal modulator backed by a dielectric mirror. The specific model used is the Boulder Non-Linear Systems XY Ferroelectric Series with amplitude only modulation. For the purposes of this research, the SLM was used to

generate static turbulence for characterization of the SRI, but it also has potential for use in closed-loop adaptive optics. The SLM is capable of up to 90 degrees of polarization rotation at 1 kHz frame rate. An image of the SLM is shown in Figure 4.

Figure 4. Spatial light modulator manufactured by Boulder Non-Linear Systems used in the experimental set-up.

WaveProp was used to generate amplitude and phase data for simulated deep turbulence effects, including scintillation and branch points. This amplitude and phase data is then implemented by the spatial light modulator (SLM) to aberrate the incident laser light [20]. The light reflected from the SLM is then representative of light that has passed through a long propagation path within a turbulent medium. For the experimental data collection, several arbitrarily selected Rytov numbers were used ranging from 0.044 to 0.410. The intent was to analyze the SRI using a wide range of values to determine if there were any trends in the behavior of the SRI at different turbulence or signal levels. The performance of the SLM in reproducing the turbulence correctly was not explicitly measured, but rather was taken as a potential source of error in the final reconstruction at the SRI.

C. SELF-REFERENCING INTERFEROMETER

Shown in Figure 5 is a detailed view of the SRI setup [21].

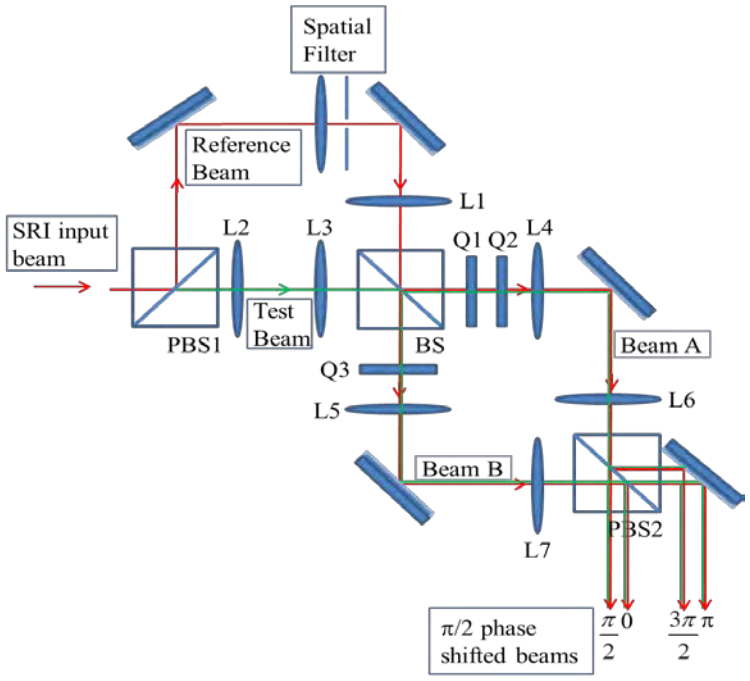

Figure 5. Optical layout of the self-referencing interferometer in the AOCoE at NPS.

A full description of this instrument was presented at the 2013 DEPS Beam Control Conference in Monterey, California [21]. The SRI is a polarization phase shifting interferometer based on a Mach-Zehnder interferometer [22], [23]. The incoming light is divided by a polarized beam splitter into two beams, a reference beam and a test beam. The reference beam is generated by placing a pinhole on the beam path that reflects from the PBS1 to spatially filter the incoming light. Lens L1 is used to collimate the reference beam. Lenses L2 and L3 are used to relay the pupil plane of the Test Beam. The beams pass through a 50/50 beam splitter and the two output beams, A and B, pass through quarter wave-plates. Lenses L4, L6 and L5, L7 are used to relay the pupil plane of beams A and B, respectively. Both beam A and beam B are composed of a reference beam and a test beam. Beam A passes through two quarter wave plates Q1 and Q2, while beam B passes through a single quarter wave-plate, Q3. The fast axis of quarter wave-plate Q1 is set at 0° and adds a π/2 phase shift. The fast axis of quarter wave-plates Q2 and Q3 are set at 45°. Wave-plate Q1 converts reference and test beam of beam A in to opposite handed circularly polarized light. Wave-plate Q3 converts beam B in to opposite handed circularly polarized light. The additional PBS1 splits beams A and B

into four beams, which are π/2 phase-shifted interferograms that are then imaged at the sensing camera. The opposite handed circularly polarized light of beam A develops π shift between the reflected and transmitted beam from the PBS1. The opposite handed circularly polarized light of beam B develops a π shift between the reflected and transmitted beam from the PBS1. The wave-front phase can be determined from the four phase-shifted images using a four bucket method, Equation 1 [22], [23].

Figure 6 shows an example of the four beams with the reference only, where the signal has been blocked, and the signal only, where the reference has been blocked. These images were collected with a 16-bit digital imaging system. The artificial color mapping from blue to red is used to create visual distinction between low and high intensity values respectively.

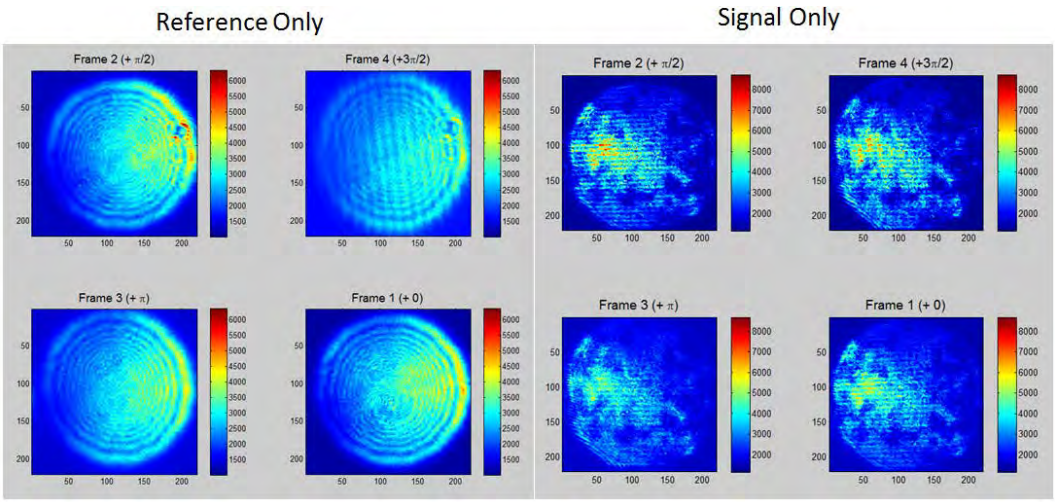

Figure 6. Image of four phase shifted reference beams, and four phase shifted signal beams before interference. Signal beams have Rytov number of 0.044.

This SRI utilizes a single digital imaging system to collect all four beams simultaneously in the same frame. This is known as spatial phase shifting. The phase of the original wave-front can then be extracted from the image of these four beams as previously explained [9].

D. CAMERA

The camera used in the experimental set-up is the ALTA U260 manufactured by Apogee Imaging Systems. This camera is specifically designed for low noise and high dynamic range for the most sensitive of scientific imaging, and is shown in Figure 7.

Figure 7. Apogee Imaging Systems ALTA U260 imaging system used in the adaptive optics test bed at NPS.

In general, the signal level tends to drop off as the level of turbulence increases. This is due to the loss of coherence in the beam, and the dispersion of energy as the beam propagates. Integration time at the camera is selected based on the need for a reasonable signal level at the highest Rytov numbers. This is expected to yield reasonable SNR for high Rytov numbers and more than sufficient SNR at lower Rytov numbers. In a closed-loop adaptive optics setup the integration time would be a small fraction of this value due to the need to correct the wave-front as the medium itself changes at a high frequency. The details of the imaging system are shown in Table 2 [17].

CCD	Kodak KAF-0261E	**Digital Resolution**	16 bits
Array Size (pixels)	512x512	**System Noise(typical)**	15 e^- RMS
Linear Full Well (typical)	500,000 electrons	**Cooling(typical)**	50 C below ambient
QE at 632nm	54%	**Dark Current(typical)**	1 e^-/pixel/sec (-25 C)

Table 2. ALTA U260 imaging system specifications.

THIS PAGE INTENTIONALLY LEFT BLANK

IV. RESULTS AND ANALYSIS

The experiment was conducted for five separate Rytov numbers ranging from 0.044 to 0.4010. This range was necessitated by the experimental set-up constraints. For Rytov numbers beyond .4 the signal level is attenuated too much to get useful results. Each experimental result will be shown with its simulated counterpart for the purpose of qualitative analysis. The measure of effectiveness of the experimental results will be based on phase reconstruction, branch point identification, and overall tilt. This data is shown in Figures 8 to 22. All phase data is reported in radians.

A. RYTOV 0.044

1. Phase reconstruction

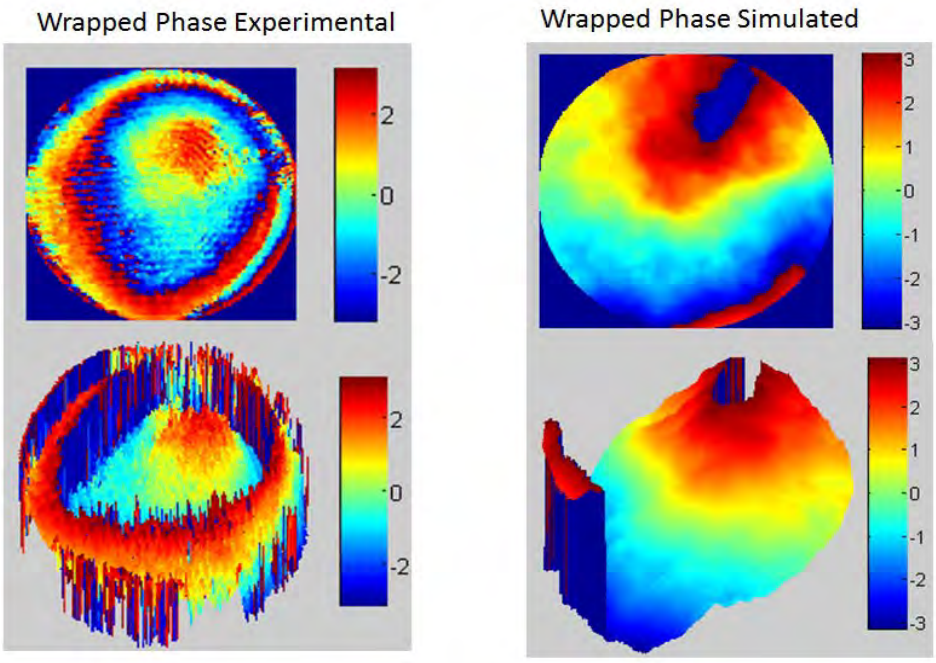

Figure 8. Reconstructed phase data for experimental and simulated cases at Rytov number 0.044.

Mismatch in the phase reconstruction can be explained by the arbitrary nature of wrapping cut placement. The data is wrapped between $-\pi$ and $+\pi$ due to the domain of the tangent function. The piston term in the wave-front will determine how far forward

or backward the wave-front is pushed, and determines where the wrapping cuts lie. In the above case the peak of the simulated data has been wrapped, but in the experimental data the peak remains intact. The clear consequence of this is that the experimental data has a wrapping cut further up the slope toward the peak of the data. There is no real impact of this phenomenon on the ability of the adaptive optics system to compensate, as piston can be easily removed by a deformable.

2. Branch Points

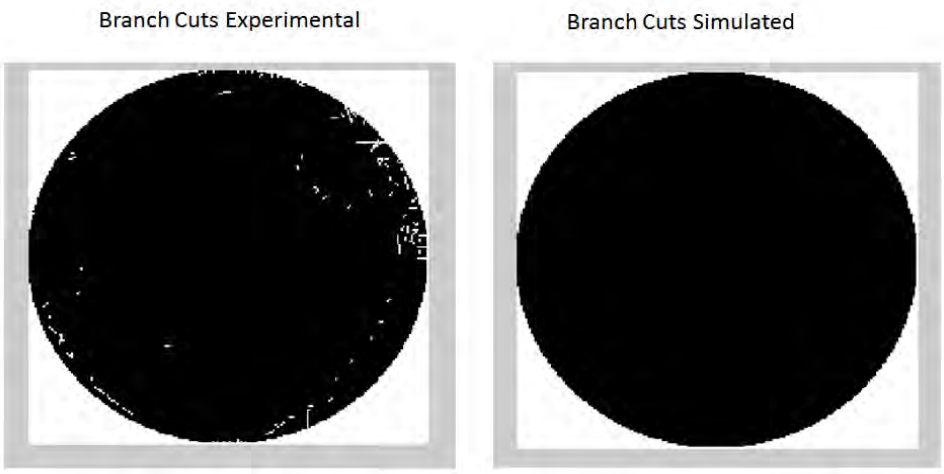

Figure 9. Branch point occurrence for experimental and simulated cases at Rytov number 0.044.

This fairly low turbulence level did not generate any branch points in the simulated data. The occurrence of branch points in the experimental data around the edges can be explained by poor quality data around the edges of the beam where there may be incomplete overlap of the reference and signal beams, or loss of signal due to optical misalignment. Branch points around the edges of the data are a common theme throughout the experiment. The quality of this reconstruction is quite good. There are very few occurrences of branch points in the center of the wave-front where the data is best.

3. Overall Tilt

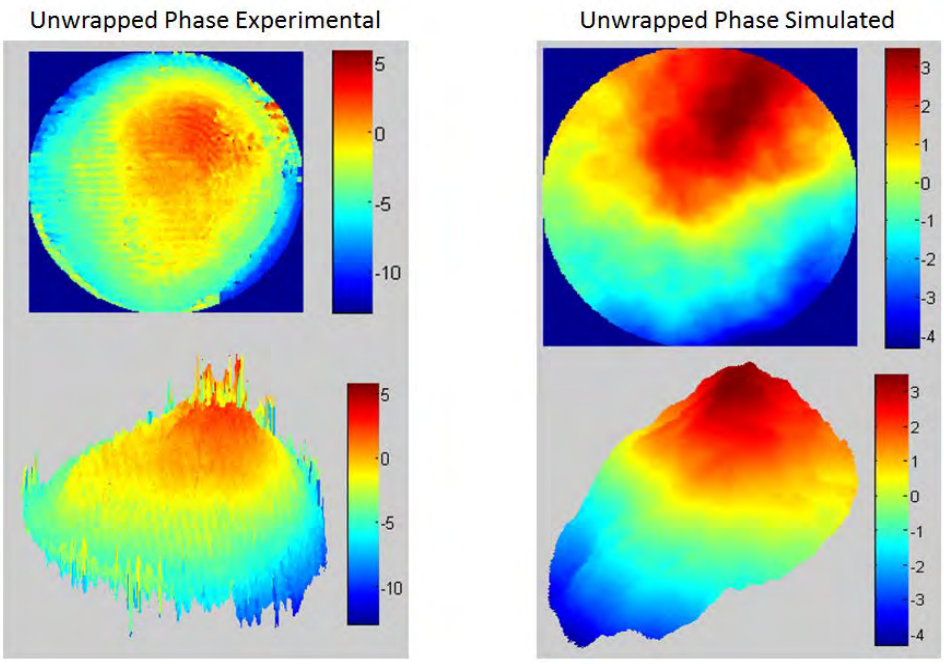

Figure 10. Unwrapped phase data for experimental and simulated cases at Rytov number 0.044.

After the phase is unwrapped the overall tip/tilt of the wave-front can be measured. Piston is still present, as in the wrapped case, but the important factor is the total range of the data. In this case the range of the experimental data is close to double that of the simulated data. Once again the edges of the data are to blame because they add high and low spikes to the data that increase the overall range. If these outliers are disregarded, the range of the two data sets is quite comparable.

B. RYTOV 0.109

1. Phase Reconstruction

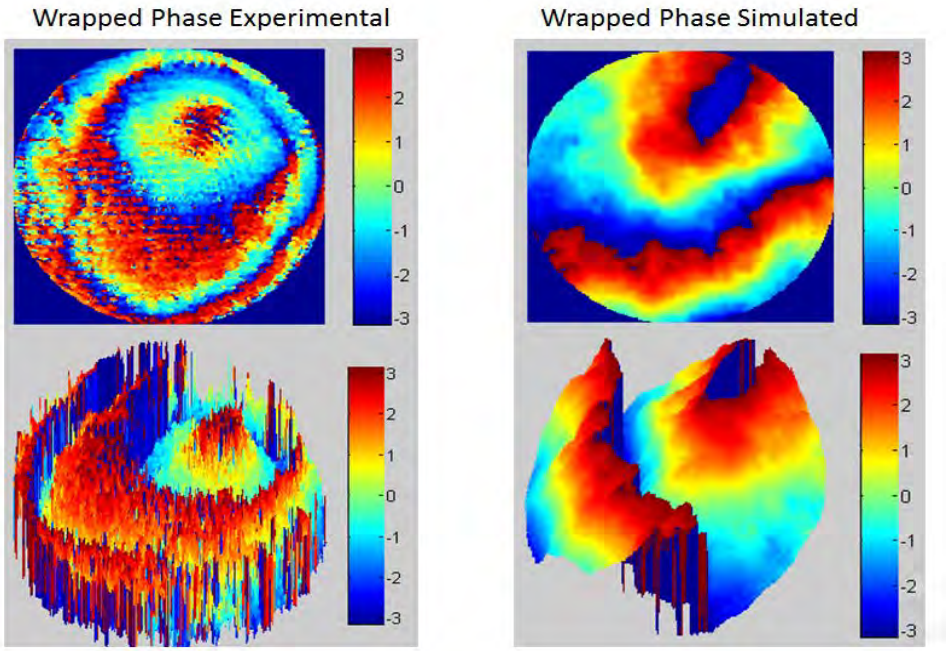

Figure 11. Reconstructed phase data for experimental and simulated cases at Rytov number 0.109.

Increasing the turbulence to 0.109 has little effect qualitatively on wave-front reconstruction. The piston term still shows itself in the variation of wrapping cuts between simulated and experimental data. The overall tilt has increased, as evidenced by encroachment of the wrapping cut.

2. Branch Points

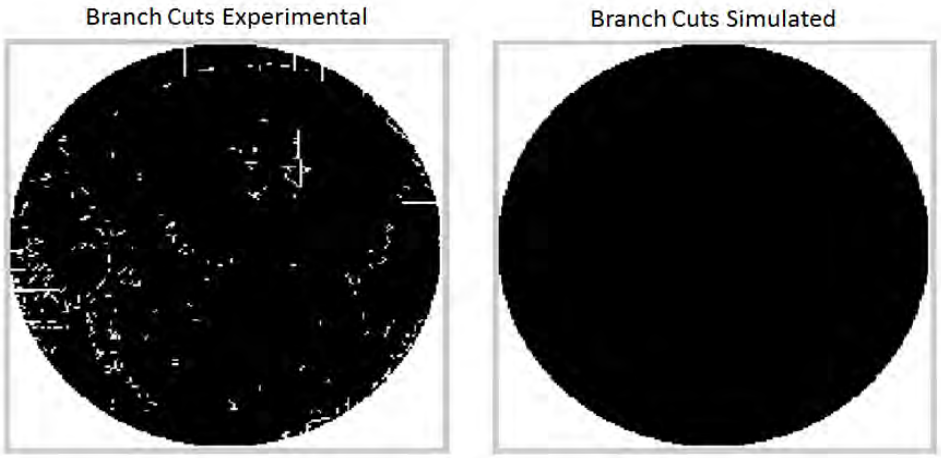

Figure 12. Branch point occurrence for experimental and simulated cases at Rytov number 0.109.

The real difference that can be seen from the increased level of turbulence is the addition of many more branch points in the experimental data, while the simulation still shows no branch cuts. A Rytov number of 0.109 is not yet within the realm of deep turbulence. As turbulence increases, error enters in the form of misregistration, signal drop-outs, and variation in alignment. Misregistration is the result of a misalignment of the four interferograms, which must be compared on a pixel by pixel basis. As turbulence increases, the effects of misregistration become more apparent because of the increased likelihood that adjacent pixels will have dramatically different phase values, and thus will skew the results if the pixels are misaligned.

3. Overall Tilt

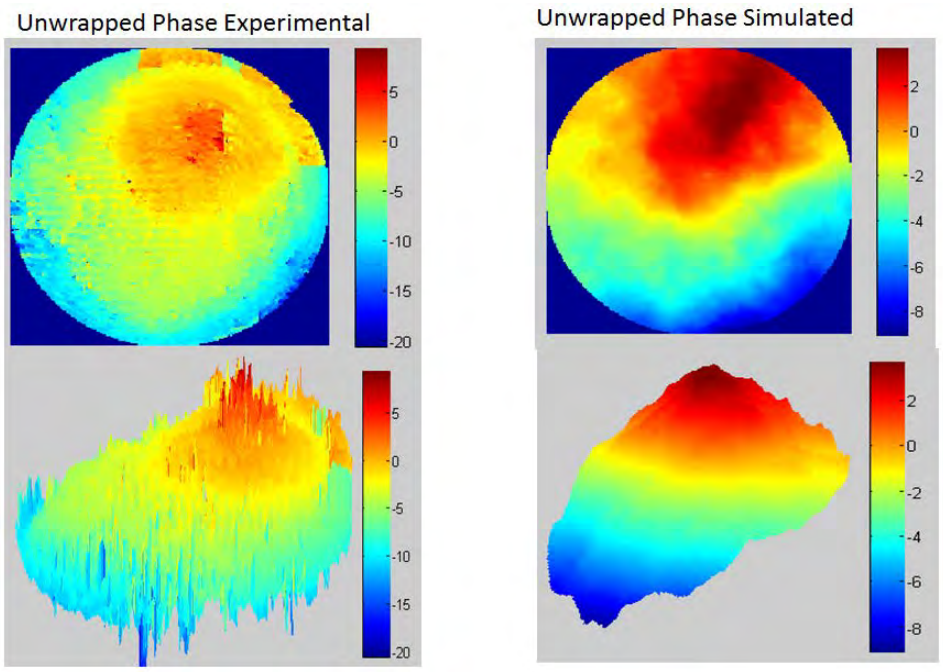

Figure 13. Unwrapped phase data for experimental and simulated cases at Rytov number 0.109.

It should be noted that the overall tilt has increased from the previous Rytov number from approximately 8 to around 12. The difference in overall tilt between the experimental and simulated data is still explained by edge effects, though with greater difficulty. The peak of the experimental data appears to be quite noisy, and the spikes there contribute more to the overall tilt than edge effects can explain.

C. RYTOV 0.205

1. Phase Reconstruction

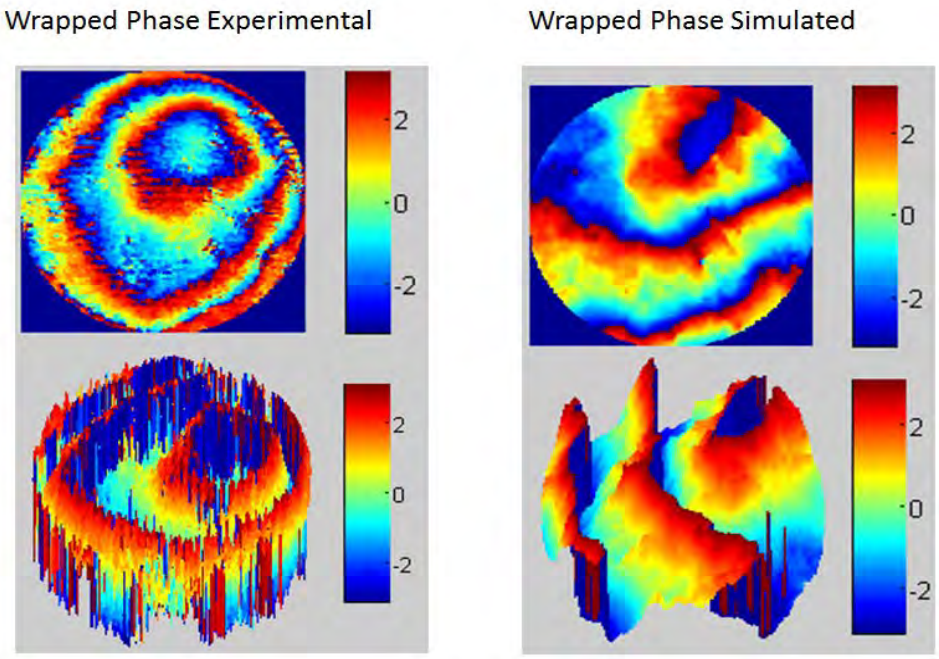

Figure 14. Reconstructed phase data for experimental and simulated cases at Rytov number 0.205.

The data shows an additional wrapping cut that was not there previously. Also, it is becoming apparent that the experimental data has a decidedly circular appearance as if the data were stretched over the surface of a sphere. This is likely due to the camera being out of the imaging plane and is known as a defocus term. This is the second order Zernike polynomial term. Otherwise, the reconstruction is qualitatively sound.

2. Branch Points

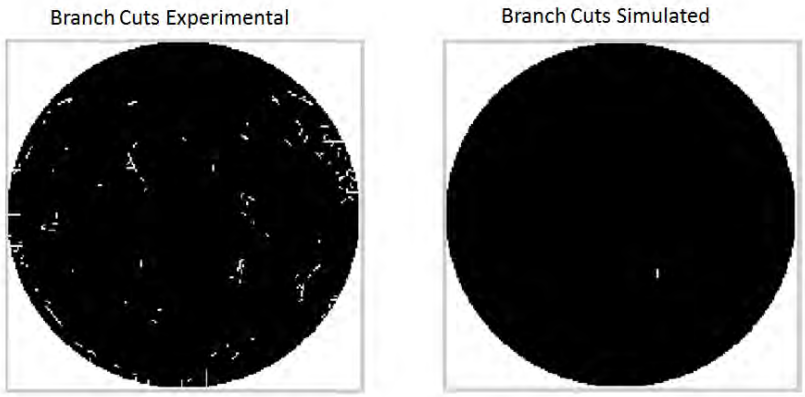

Figure 15. Branch point occurrence for experimental and simulated cases at Rytov number 0.205.

This Rytov number marks the appearance of a branch point in the simulated data. There are still far more branch points in the experimental data, further reinforcing the suspicion that various types of error have crept in.

3. Overall Tilt

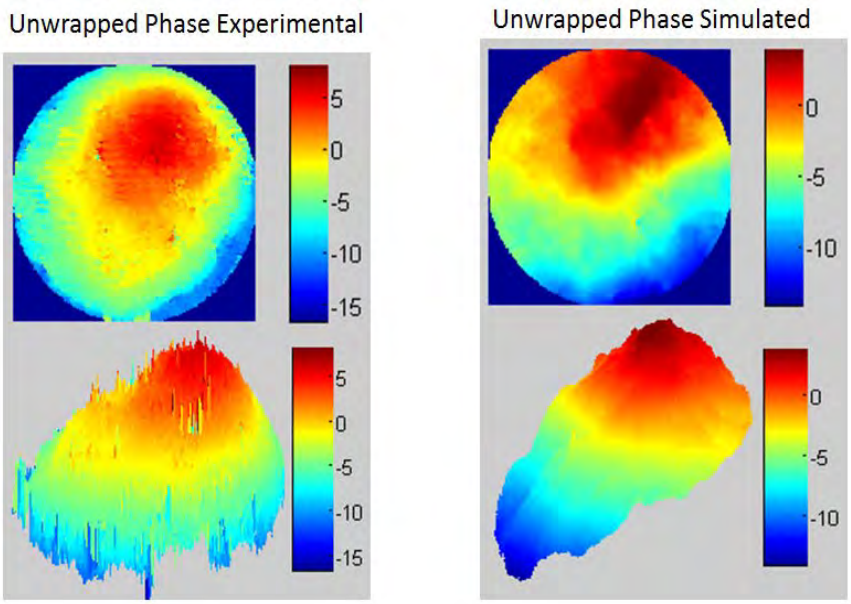

Figure 16. Unwrapped phase data for experimental and simulated cases at Rytov number 0.205.

D. RYTOV 0.301

1. Phase Reconstruction

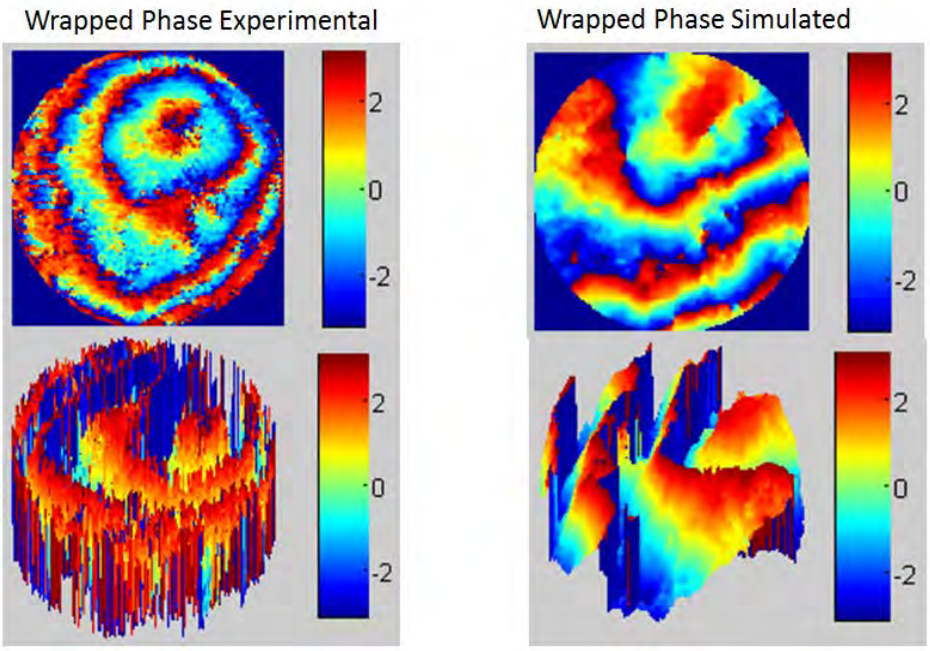

Figure 17. Reconstructed phase data for experimental and simulated cases at Rytov number 0.301.

2. Branch Points

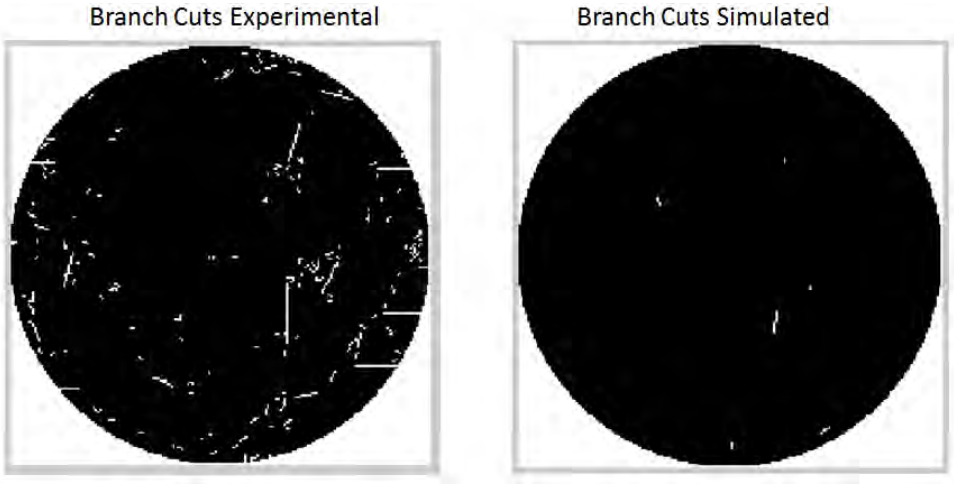

Figure 18. Branch point occurrence for experimental and simulated cases at Rytov number 0.301.

The increased level of turbulence is responsible for the appearance of even more branch points in the simulated data. The turbulence is now clearly within the deep turbulence regime. The number of branch points in the experimental data has not significantly increased, which may indicate the experimental data is showing resilience to increased turbulence levels. There are for the first significant branch cuts, which pose a problem for traditional reconstructors, but not for the SRI.

3. Overall Tilt

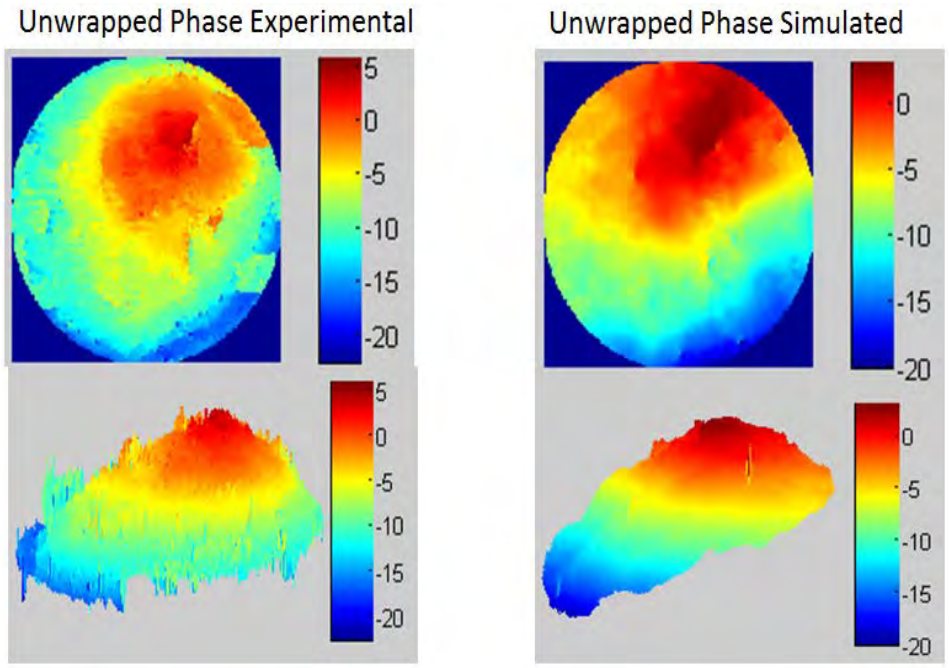

Figure 19. Unwrapped phase data for experimental and simulated cases at Rytov number 0.301.

The experimental and simulated data are remarkably close in overall tilt. As with the branch point analysis, this may indicate the experimental set-up is showing resilience to increased levels of turbulence.

E. RYTOV 0.401

1. Phase Reconstruction

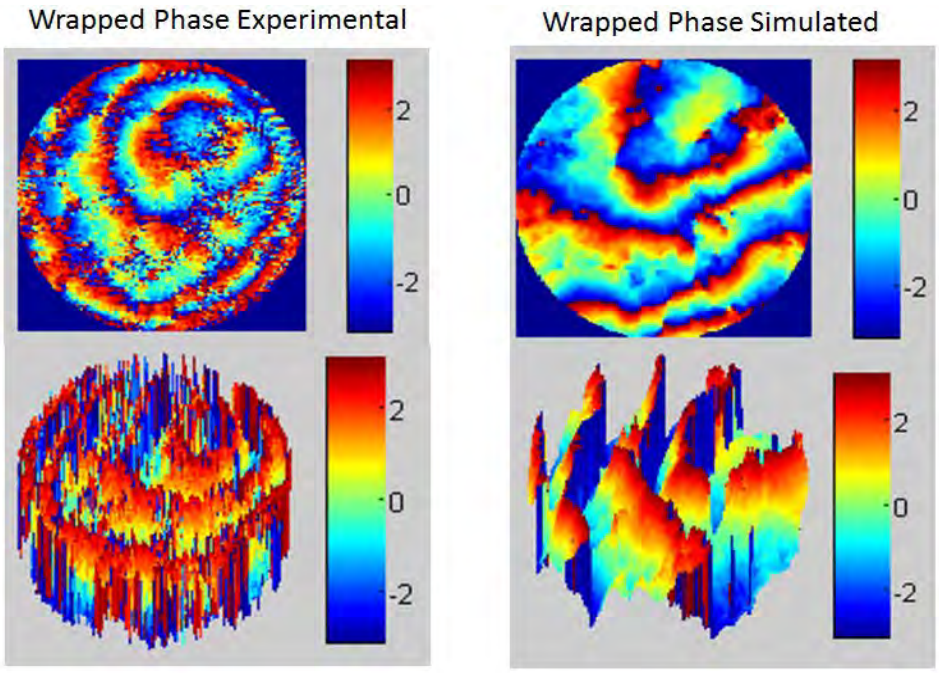

Figure 20. Reconstructed phase data for experimental and simulated cases at Rytov number 0.401.

The final data set is the highest level of turbulence that was examined. The number of wrapping cuts has again increased indicating an increase in overall tilt.

2. Branch Points

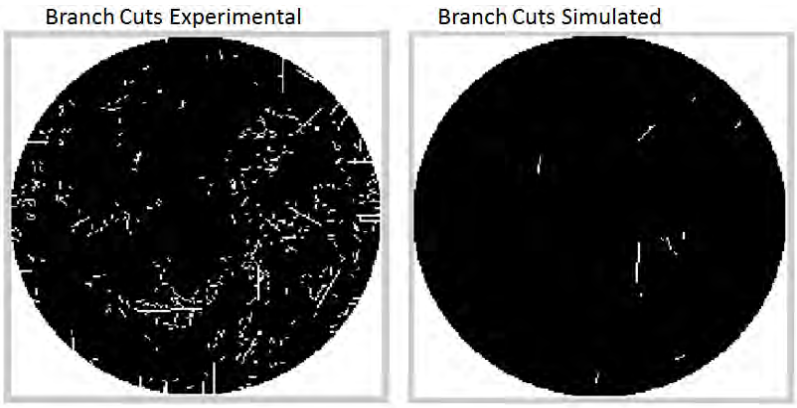

Figure 21. Branch point occurrence for experimental and simulated cases at Rytov number 0.401.

There is clearly a large increase in branch points in this data set. The experimental data has exploded with branch points, while the simulated data has a modest increase. The experimental data is nearing the verge of its capability to reproduce the wave-front accurately.

3. Overall Tilt

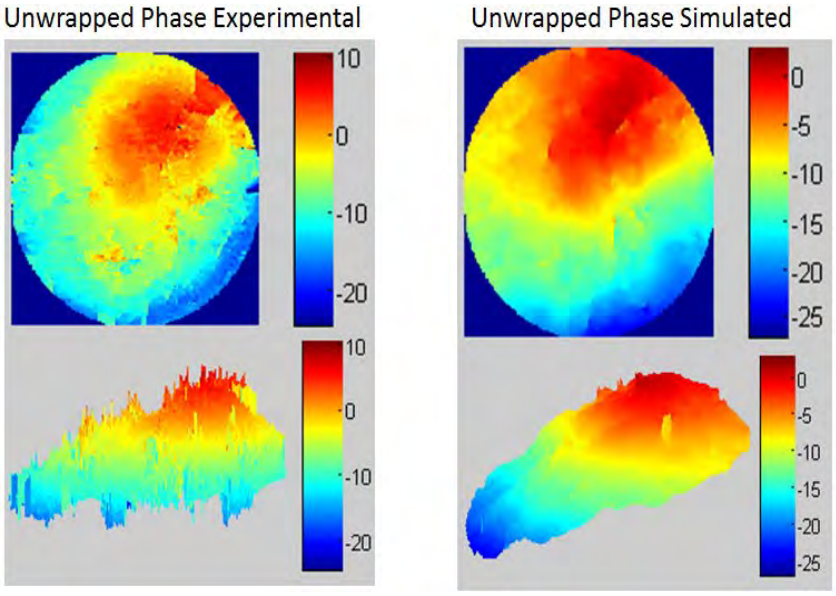

Figure 22. Unwrapped phase data for experimental and simulated cases at Rytov number 0.401.

V. CONCLUSION

The SRI was successfully developed at the Naval Postgraduate School. A qualitative analysis of the phase reconstruction in the experimental results shows a remarkable resemblance to the phase reconstruction in the simulated results. Also, upon comparison of the unwrapped phase between the experimental results and the simulated results, the overall tip and tilt of the wave-front is found to be comparable, neglecting outliers. Finally, the few branch points that do appear in the simulated results can also be identified in the experimental results. The similarity of these features between the ideal simulation and the experimentation demonstrates the success of the experimental set-up. While there is still significant work to be done in making improvements to the quality of the reconstruction and the level of turbulence the system can handle, the instrument already has a baseline capability to reconstruct wave-fronts with simulated deep turbulence effects. Simulated results show a significant drop-off in Strehl ratio below a SNR of two. The system is limited in the level of turbulence that can be accurately processed due to loss of signal strength at the sensor. Beyond a Rytov number of 0.4, the system creeps out of alignment and the reconstruction can no longer be completed because of diminishing SNR.

Further improvements need to be made to the instrument before it can be used in closed-loop adaptive optics and beam correction. Further characterization should be done on the spatial light modulator, and an effort made to identify error sources in the simulation of deep turbulence. The system as a whole should have its alignment verified and brought into focus to eliminate Fresnel ringing in the reference path, and to bring the camera into the focal plane of the interferogram. Consideration should be given to replacing the spatial filter with a single-mode optical amplifier for amplification of the reference path. This should also reduce the systems sensitivity to overall tip and tilt in the signal, which alters the alignment of the beam and causes it to “miss” the spatial filter on the reference path of the SRI.

Future work includes using closing the adaptive optics loop with a deformable mirror to apply beam correction, incorporating a Shack-Hartmann WFS to compliment

the SRI, testing the SRI with higher levels of turbulence, and developing control algorithms for the deformable mirror that are specifically designed for SRI phase reconstruction data.

APPENDIX

A. THESIS MAIN SCRIPT

```
close all;
clear all;
clc;


%DATA FORMATTING
%-------------------------------------------------------------------------
---%
%Experimental Data
%Pass along the image you wish to parse from the workspace:
load('S:\MATLAB\Thesis\Experimental_Data_Final.mat')
Rytov = 0.401;
[F1_Exp,F2_Exp,F3_Exp,F4_Exp,dim] = Manual_Acquire(Rytov_0401_Both);
%---------------------------
%Simulated Data
%Pass along Rytov number of requested data from following list:
% 0.044; 0.109; 0.205; 0.301; 0.401; 0.610; 1.090; 1.308; 1.613; 2.092;
% 2.310; 2.615; 3.051; 3.313; 3.618; 4.010
[F1_Sim,F2_Sim,F3_Sim,F4_Sim,AMP_Sim,PHA_Sim] = SRI_Sim(Rytov,dim);
%---------------------------
%Camera Noise
SNR = 4;
[F1_Sim,N1] = Noise(1e-3,F1_Sim,SNR);
[F2_Sim,N2] = Noise(1e-3,F2_Sim,SNR);
[F3_Sim,N3] = Noise(1e-3,F3_Sim,SNR);
[F4_Sim,N4] = Noise(1e-3,F4_Sim,SNR);
%Plot_Frames(N1,N2,N3,N4)
%---------------------------
%Generate Frame Plots
Plot_Frames(F1_Exp,F2_Exp,F3_Exp,F4_Exp)
Plot_Frames(F1_Sim, F2_Sim,F3_Sim,F4_Sim)
%---------------------------
%Four Bucket Method
Phase_Wrapped_Exp = atan2((F4_Exp - F2_Exp),(F1_Exp - F3_Exp));
Phase_Wrapped_Sim = atan2((F4_Sim - F2_Sim),(F1_Sim - F3_Sim));
Complex_Wave_Exp = AMP_Sim.*exp(j.*Phase_Wrapped_Exp);
Complex_Wave_Sim = AMP_Sim.*exp(j.*Phase_Wrapped_Sim);
%-------------------------------------------------------------------------
---%


%STREHL RATIO COMPUTATION
%-------------------------------------------------------------------------
---%
Uorig = AMP_Sim.*exp(j.*PHA_Sim);
Urec_Sim = exp(-j.*Phase_Wrapped_Sim);

%how well I reconstructed the phase, not as meaningful for real data
```

```
%because I don't have the original phase/amp for this data set.  Always
one
%if no noise added.
Strehl_Reconstructor_Sim =
(abs(sum(sum(Uorig.*Urec_Sim)))^2)/(sum(sum(abs(Uorig))))^2;
%-------------------------------------------------------------------------
---%


%UNWRAP
%-------------------------------------------------------------------------
---%
%Unwrap Mask
%Select circular mask or square mask for unwrapping
    %For square mask set mask_flag = 0;
    %For circular mask set mask_flag = 1;
mask_flag = 1;

if (mask_flag == 0)
    Mask = ones(dim);
end
if (mask_flag == 1)
    Mask = zeros(dim);
    for i= 1:dim
        for j = 1:dim
            r =  norm([round(dim/2) round(dim/2)]-[i j]);
            if (r < dim/2)
                Mask(i,j) = 1;
            end
        end
    end
end
%--------------------------
%Unwrap Algorithm
%Unwrap the Phase using one of the below algorithms
%For Quality Guided 2D Unwrap method = 1;
%For Goldstein 2D Unwrap method = 2;
%For Constantini Network Programming 2D Unwrap method = 3;
method = 2;

Phase_Unwrapped_Sim = Phase_Unwrap( Complex_Wave_Sim, Mask, method);
Phase_Unwrapped_Exp = Phase_Unwrap(Complex_Wave_Exp, Mask, method);
%-------------------------------------------------------------------------
---%
```

B. FRAME ACQUISITION FUNCTION

```
function [F1,F2,F3,F4,dim] = Manual_Acquire(Im_in)
%MANUAL_ACQUIRE Takes in the full camera image and return 4 sub frames.
    %The frames have been adjusted for beam size, beam shape,
    %and average intensity.
```

```
%specify the image you wish to process
Image = Im_in;


%Begin Frame Grabbing

%Optimized for New SLM image, must re-optimize for new alignment
F3 = Image(35:242,270:467);
F4 = Image(50:260,56:254);
F2 = Image(282:495,73:268);
F1 = Image(262:475,295:500);
dim = 200;


F1 = imresize(F1, [dim dim]);
F2 = imresize(F2, [dim dim]);
F3 = imresize(F3, [dim dim]);
F4 = imresize(F4, [dim dim]);
IM_mask = zeros(dim);
for i= 1:dim
    for j = 1:dim
        r =  norm([round(dim/2) round(dim/2)]-[i j]);
        if (r < dim/2)
            IM_mask(i,j) = 1;
        end
    end
end
%normalize the average intensity of the four frames.
F1_temp = F1.*IM_mask;
F2_temp = F2.*IM_mask;
F3_temp = F3.*IM_mask;
F4_temp = F4.*IM_mask;

F1_sum = sum(sum(F1_temp));
F2_sum = sum(sum(F2_temp));
F3_sum = sum(sum(F3_temp));
F4_sum = sum(sum(F4_temp));

F1_avg = F1_sum /(pi*(dim/2)^2);
F2_avg = F2_sum /(pi*(dim/2)^2);
F3_avg = F3_sum /(pi*(dim/2)^2);
F4_avg = F4_sum /(pi*(dim/2)^2);

Avg_avg = (F1_avg + F2_avg + F3_avg + F4_avg)/4;

F1 = F1.*Avg_avg./F1_avg;
F2 = F2.*Avg_avg./F2_avg;
F3 = F3.*Avg_avg./F3_avg;
F4 = F4.*Avg_avg./F4_avg;

end
```

C. SRI SIMULATOR FUNCTION

```
function [ F1,F2,F3,F4,AMP,PHA ] = SRI_Sim( Rytov,dim )
    %SRI_SIM Summary of this function goes here
    %   Detailed explanation goes here

    load('S:\MATLAB\Thesis\Simulation_Data_Final.mat')


%The following data is used in the simulation and experimentation
portion
%of the Experiment
%%%%%%%%%%%%%%%%%%%%%%%%%%%%%%%%%%%%%%%%%%%%%%%%%%%%%%%%%%%%%%%%%%%%%%%%
%%%%
    %Rytov 0.044
    if (Rytov == 0.044)
        F1 = AMP_0044 + AMP_0044.*cos(PHA_0044);
        F2 = AMP_0044 - AMP_0044.*sin(PHA_0044);
        F3 = AMP_0044 - AMP_0044.*cos(PHA_0044);
        F4 = AMP_0044 + AMP_0044.*sin(PHA_0044);
        AMP = AMP_0044;
        PHA = PHA_0044;
    end

    %Rytov 0.109
    if (Rytov == 0.109)
        F1 = AMP_0109 + AMP_0109.*cos(PHA_0109);
        F2 = AMP_0109 - AMP_0109.*sin(PHA_0109);
        F3 = AMP_0109 - AMP_0109.*cos(PHA_0109);
        F4 = AMP_0109 + AMP_0109.*sin(PHA_0109);
        AMP = AMP_0109;
        PHA = PHA_0109;
    end

     %Rytov 0.205
    if (Rytov == 0.205)
        F1 = AMP_0205 + AMP_0205.*cos(PHA_0205);
        F2 = AMP_0205 - AMP_0205.*sin(PHA_0205);
        F3 = AMP_0205 - AMP_0205.*cos(PHA_0205);
        F4 = AMP_0205 + AMP_0205.*sin(PHA_0205);
        AMP = AMP_0205;
        PHA = PHA_0205;
    end

    %Rytov 0.301
    if (Rytov == 0.301)
        F1 = AMP_0301 + AMP_0301.*cos(PHA_0301);
        F2 = AMP_0301 - AMP_0301.*sin(PHA_0301);
        F3 = AMP_0301 - AMP_0301.*cos(PHA_0301);
        F4 = AMP_0301 + AMP_0301.*sin(PHA_0301);
        AMP = AMP_0301;
        PHA = PHA_0301;
    end
```

```
    %Rytov 0.401
    if (Rytov == 0.401)
        F1 = AMP_0401 + AMP_0401.*cos(PHA_0401);
        F2 = AMP_0401 - AMP_0401.*sin(PHA_0401);
        F3 = AMP_0401 - AMP_0401.*cos(PHA_0401);
        F4 = AMP_0401 + AMP_0401.*sin(PHA_0401);
        AMP = AMP_0401;
        PHA = PHA_0401;
    end
%%%%%%%%%%%%%%%%%%%%%%%%%%%%%%%%%%%%%%%%%%%%%%%%%%%%%%%%%%%%%%%%%%%%%%%%%
%%%%

%The following data is used only in the Simulation portion of the
%Experiment
    %Rytov 0.610
    if (Rytov == 0.610)
        F1 = AMP_0610 + AMP_0610.*cos(PHA_0610);
        F2 = AMP_0610 - AMP_0610.*sin(PHA_0610);
        F3 = AMP_0610 - AMP_0610.*cos(PHA_0610);
        F4 = AMP_0610 + AMP_0610.*sin(PHA_0610);
        AMP = AMP_0610;
        PHA = PHA_0610;
    end

    %Rytov 1.090
    if (Rytov == 1.090)
        F1 = AMP_1090 + AMP_1090.*cos(PHA_1090);
        F2 = AMP_1090 - AMP_1090.*sin(PHA_1090);
        F3 = AMP_1090 - AMP_1090.*cos(PHA_1090);
        F4 = AMP_1090 + AMP_1090.*sin(PHA_1090);
        AMP = AMP_1090;
        PHA = PHA_1090;
    end

    %Rytov 1.308
    if (Rytov == 1.308)
        F1 = AMP_1308 + AMP_1308.*cos(PHA_1308);
        F2 = AMP_1308 - AMP_1308.*sin(PHA_1308);
        F3 = AMP_1308 - AMP_1308.*cos(PHA_1308);
        F4 = AMP_1308 + AMP_1308.*sin(PHA_1308);
        AMP = AMP_1308;
        PHA = PHA_1308;
    end

    %Rytov 1.613
    if (Rytov == 1.613)
        F1 = AMP_1613 + AMP_1613.*cos(PHA_1613);
        F2 = AMP_1613 - AMP_1613.*sin(PHA_1613);
        F3 = AMP_1613 - AMP_1613.*cos(PHA_1613);
        F4 = AMP_1613 + AMP_1613.*sin(PHA_1613);
        AMP = AMP_1613;
        PHA = PHA_1613;
    end
```

```
%Rytov 2.092
if (Rytov == 2.092)
    F1 = AMP_2092 + AMP_2092.*cos(PHA_2092);
    F2 = AMP_2092 - AMP_2092.*sin(PHA_2092);
    F3 = AMP_2092 - AMP_2092.*cos(PHA_2092);
    F4 = AMP_2092 + AMP_2092.*sin(PHA_2092);
    AMP = AMP_2092;
    PHA = PHA_2092;
end

%Rytov 2.310
if (Rytov == 2.310)
    F1 = AMP_2310 + AMP_2310.*cos(PHA_2310);
    F2 = AMP_2310 - AMP_2310.*sin(PHA_2310);
    F3 = AMP_2310 - AMP_2310.*cos(PHA_2310);
    F4 = AMP_2310 + AMP_2310.*sin(PHA_2310);
    AMP = AMP_2310;
    PHA = PHA_2310;
end

%Rytov 2.615
if (Rytov == 2.615)
    F1 = AMP_2615 + AMP_2615.*cos(PHA_2615);
    F2 = AMP_2615 - AMP_2615.*sin(PHA_2615);
    F3 = AMP_2615 - AMP_2615.*cos(PHA_2615);
    F4 = AMP_2615 + AMP_2615.*sin(PHA_2615);
    AMP = AMP_2615;
    PHA = PHA_2615;
end

%Rytov 3.051
if (Rytov == 3.051)
    F1 = AMP_3051 + AMP_3051.*cos(PHA_3051);
    F2 = AMP_3051 - AMP_3051.*sin(PHA_3051);
    F3 = AMP_3051 - AMP_3051.*cos(PHA_3051);
    F4 = AMP_3051 + AMP_3051.*sin(PHA_3051);
    AMP = AMP_3051;
    PHA = PHA_3051;
end

%Rytov 3.313
if (Rytov == 3.313)
    F1 = AMP_3313 + AMP_3313.*cos(PHA_3313);
    F2 = AMP_3313 - AMP_3313.*sin(PHA_3313);
    F3 = AMP_3313 - AMP_3313.*cos(PHA_3313);
    F4 = AMP_3313 + AMP_3313.*sin(PHA_3313);
    AMP = AMP_3313;
    PHA = PHA_3313;
end

%Rytov 3.618
if (Rytov == 3.618)
    F1 = AMP_3618 + AMP_3618.*cos(PHA_3618);
    F2 = AMP_3618 - AMP_3618.*sin(PHA_3618);
```

```
        F3 = AMP_3618 - AMP_3618.*cos(PHA_3618);
        F4 = AMP_3618 + AMP_3618.*sin(PHA_3618);
        AMP = AMP_3618;
        PHA = PHA_3618;
    end

    %Rytov 4.010
    if (Rytov == 4.010)
        F1 = AMP_4010 + AMP_4010.*cos(PHA_4010);
        F2 = AMP_4010 - AMP_4010.*sin(PHA_4010);
        F3 = AMP_4010 - AMP_4010.*cos(PHA_4010);
        F4 = AMP_4010 + AMP_4010.*sin(PHA_4010);
        AMP = AMP_4010;
        PHA = PHA_4010;
    end
%%%%%%%%%%%%%%%%%%%%%%%%%%%%%%%%%%%%%%%%%%%%%%%%%%%%%%%%%%%%%%%%%%%%%%%%%%%%%%%
%%%%
%Resize and mirror data to more closely match experimental data
F1 = imresize(F1, [dim dim]);
F2 = imresize(F2, [dim dim]);
F3 = imresize(F3, [dim dim]);
F4 = imresize(F4, [dim dim]);
AMP = imresize(AMP, [dim dim]);
PHA = imresize(PHA, [dim dim]);
Temp1 = zeros(dim);
Temp2 = zeros(dim);
Temp3 = zeros(dim);
Temp4 = zeros(dim);
Temp5 = zeros(dim);
Temp6 = zeros(dim);
for i = 1:dim
    Temp1(:,i) = F1(:,abs(i-(dim+1)));
    Temp2(:,i) = F2(:,abs(i-(dim+1)));
    Temp3(:,i) = F3(:,abs(i-(dim+1)));
    Temp4(:,i) = F4(:,abs(i-(dim+1)));
    Temp5(:,i) = AMP(:,abs(i-(dim+1)));
    Temp6(:,i) = PHA(:,abs(i-(dim+1)));
end
F1 = Temp1;
F2 = Temp2;
F3 = Temp3;
F4 = Temp4;
AMP = Temp5;
PHA = Temp6;

end
```

D. NOISE FUNCTION

```
function [ Noisy_Image, Noise_Frame] = Noise( Int_time,Image,SNR)

%NOISE :  Noise modeled after the ALTA U260 camera from Apogee Imaging
% Systems, which contains the KAF-0261 CCD from TrueSense imaging, inc.
% This imaging system is a cooled system, with low noise, and high
dynamic
```

```
% range.
%Definition of noise in this case is SNR = mu/sigma, which is the
%mean of the signal divided by the std dev of the noise.
%Define Camera Parameters
[rows,~] = size(Image);
signal_average = sum(sum(Image))/rows^2;
sigma_total_noise = signal_average/SNR; %this includes all system noise
dark_current_rate = 10; %this is for -25 C
non_uniformity = .05; %standard deviation is 5% of pixel value

[rows,~] = size(Image);

dark_current_frame = zeros(rows)+ dark_current_rate*Int_time;

bias_frame = sigma_total_noise.*randn(rows);

non_uniform = 1 + non_uniformity.*randn(rows);

Noise_Frame = dark_current_frame + bias_frame;
Noisy_Image = Image.*non_uniform + Noise_Frame;
```

E. 2D PHASE UNWRAP FUNCTION

```
%%%%%%%%%%%%%%%%%%%%%%%%%%%%%%%%%%%%%%%%%%%%%%%%%%%%%%%%%%%%%%%%%%%%%%%%%
%%%%%%%%%%%%%%%%%%%%%%%%%%%%%%%%%
% GoldsteinUnwrap2D is a script to demonstrate the 2D Goldstein branch
cut phase unwrapping algorithm.
%
%  Calls: PhaseResidues
%         BranchCuts
%         FloodFill
%
% References::
% 1. R. M. Goldstein, H. A. Zebken, and C. L. Werner, “Satellite radar
interferometry:
%    Two-dimensional phase unwrapping,” Radio Sci., vol. 23, no. 4, pp.
713–720, 1988.
% 2. D. C. Ghiglia and M. D. Pritt, Two-Dimensional Phase Unwrapping:
%    Theory, Algorithms and Software. New York: Wiley-Interscience,
1998.
%
% Inputs:  1. IM = Complex image
%  Optional inputs:
%          2. im_mask = Binary mask
%          3. max_box_radius= Maximum search box radius (pixels)
%          4. threshold_std = Number of noise standard deviations used
for
%          thresholding the magnitude image
% Outputs: 1. Unwrapped phase image
%          2. Phase quality map
%
% This code can easily be extended for 3D phase unwrapping.
%
% Posted by Bruce Spottiswoode on 22 December 2008
```

```
%
% 2010/07/23  Modified by Carey Smith
%             1. Changed IM_mask, IM_mag, IM_phase to lowercase, in
order to be
%                similar to the Quality Guided routines.
%             2. Moved the logic to chose the reference point from
FloodFill.m
%                to here, in order to be similar to the Quality Guided
routines.
%                The coordinates of the reference point, colref,
rowref, are now
%                passed to FloodFill2.m
%             3. User can optionally have the code automatically chose
the
%             largest magnatude point as the reference point.
%             4. Allowed the user to specify IM, im_mask,
max_box_radius before
%                calling this routine.  (Note that threshold_std is not
used.)
%             5. Modified the plots to suit my preferences.
%
%%%%%%%%%%%%%%%%%%%%%%%%%%%%%%%%%%%%%%%%%%%%%%%%%%%%%%%%%%%%%%%%%%%%%%%
%%%%%%%%%%%%%%%%%%%%%%%%%%%%%%%


IM = Complex_Wave;
im_mag   = abs(IM);                  %Magnitude image
im_phase = angle(IM);                %Phase image

%% Replace with your mask (if desired)
im_mask = Mask;
mag_max = max(im_mag(:));
%indx1 = find(im_mag < 0.1*mag_max);  %Intensity = mag^2, so this = .04
threshold on the intensity
%im_mask(indx1) = 0;   % Don't mask at this point; wait until residues
are computed
if(~exist('im_mask','var'))
  im_mask = ones(size(IM));          %Mask (if applicable)
end
figure; imagesc(im_mag.*im_mask),   colormap(gray), axis square, axis
off, title('GS Initial masked magnitude'); colorbar;
figure; imagesc(im_phase.*im_mask), colormap(gray), axis square, axis
off, title('GS Initial masked phase'); colorbar;

%% Compute the residues
residue_charge = PhaseResidues_r1(im_phase, im_mask); % Calculate phase
residues (Does not use mask)
figure; imagesc(residue_charge), colormap(gray), axis square, axis off,
title('GS Phase residues (charged)'); colorbar;

%% Compute the branch cuts
max_box_radius=floor(length(residue_charge)/2);  % Maximum search box
radius (pixels)
%max_box_radius=4  % Maximum search box radius (pixels)
```

```
if(~exist('max_box_radius','var'))
  max_box_radius=4;  % Maximum search box radius (pixels)
end
% BranchCuts() ignores residues with mask == 0, so keep the entire mask
== 1
branch_cuts = BranchCuts_r1(residue_charge, max_box_radius, im_mask); %
Place branch cuts
figure; imagesc(branch_cuts),    colormap(gray), axis square, axis off,
title('GS Branch cuts'); colorbar;

im_mask(branch_cuts) = 0;  % Now need to mask off branch cut points, in
order to avoid an error in FloodFill
im_mag1 = im_mag.*im_mask; % Mask off magnitude == 0 points, so that
they are not chosen for the starting point

%% Manually (default) or automatically identify starting seed point
if(1)  % Chose starting point interactively
  im_phase_quality = im_mag1;
  minp = im_phase_quality(2:end-1, 2:end-1); minp = min(minp(:));
  maxp = im_phase_quality(2:end-1, 2:end-1); maxp = max(maxp(:));
  figure; imagesc(im_phase_quality,[minp maxp]), colormap(gray),
colorbar, axis square, axis off; title('Phase quality map');
  %uiwait(msgbox('Select known true phase reference phase point. Black
= high quality phase; white = low quality phase.','Phase reference
point','modal'));
  uiwait(msgbox('Select known true phase reference phase point. White =
high magnitude; Black = low magnitude.','Phase reference
point','modal'));
  [xpoint,ypoint] = ginput(1);        %Select starting point for the
guided floodfill algorithm
  colref = round(xpoint);
  rowref = round(ypoint);
  close;                              %Close the figure;
else   % Chose starting point = max. intensity
  [r_dim, c_dim]=size(im_phase);
  im_mag1(1,:) = 0;                     %Set magnitude of border pixels
to 0, so that they are not used for the reference
  im_mag1(r_dim,:) = 0;
  im_mag1(:,1) = 0;
  im_mag1(:,c_dim) = 0;
  [rowrefn,colrefn] = find(im_mag1 >= 0.99*mag_max);
  rowref = rowrefn(1);                  %Choose the 1st point for a
reference (known good value)
  colref = colrefn(1);                  %Choose the 1st point for a
reference (known good value)
end

%% Unwrap
if(exist('rowref','var'))
  im_unwrapped = FloodFill_r1(im_phase, im_mag, branch_cuts, im_mask,
colref, rowref); % Flood fill phase unwrapping
else
  im_unwrapped = FloodFill_r1(im_phase, im_mag, branch_cuts, im_mask);
% Flood fill phase unwrapping
end
```

```
% Display results
figure; imagesc(im_unwrapped), colormap(gray), colorbar, axis square,
axis off, title('GS Unwrapped phase');
```

THIS PAGE INTENTIONALLY LEFT BLANK

LIST OF REFERENCES

[1] C. Bolkcom and S. A. Hildreth, "Airborne laser (ABL): Issues for Congress," Congressional Research Service, Washington, DC, 2008.

[2] Missile Defense Agency. (Sep 2013). "ABL MDA fact sheet.pdf." [Online]. http:\\www.mda.mil.

[3] R. O'Rourke, "Navy shipboard lasers for surface, air, and missile defense: background and issues for Congress." Congressional Research Service, Washington, DC, Aug 2013.

[4] C. N. Ang, "Analysis of high energy laser weapon employment from a Navy ship," M.S. thesis, Naval Postgraduate School, Monterey, CA, 2012.

[5] Defense Science Board Task Force, "High Energy Laser Weapon Systems Applications." Defense Science Board, Washington, DC, Jun 2001.

[6] V. I. Tatarskii, "Review of scintillation phenomena in wave propagation in random media (scintillation)," SPIE, Bellingham, WA and IOP, London, 1993.

[7] F. L. Pedrotti and L. S. Pedrotti, *Introduction to optics*. Englewood Cliffs, NJ: Prentice Hall, 1993.

[8] R. Tyson, *Introduction to Adaptive Optics*. Bellingham, WA: SPIE Press, 2000.

[9] T. A. Rhoadarmer, "Development of the self-referencing interferometer wavefront sensor," in *Proceedings of SPIE, Advanced Wavefront control methods, Devices, and Application II*, vol. 5553, pp. 112–126.

[10] D. L. Fried and J. L. Vaughn, "Branch cuts in the phase function," *Appl. Opt.*, vol. 31, no. 15, pp. 2865–82, May 1992.

[11] D. L. Fried, "Branch point problem in adaptive optics," *J. Opt. Soc. Am. A*, vol. 15, no. 10, pp. 2759–2768, 1998.

[12] T. Martinez, private communication, Dec 2013.

[13] R. K. Tyson, *Principles of Adaptive Optics*, 3rd ed. Boca Raton, FL: CRC Press, 2011.

[14] C. Joenathan, "Phase-measuring interferometry: new methods and error analysis," *Appl. Opt.*, vol. 33, no. 19, pp. 4147–4155, Jul 1994.

[15] T. M. Venema and J. D. Schmidt, "Optical phase unwrapping in the presence of branch points," *Opt. Express*, vol. 16, no. 10, pp. 6985–6988, May 2008.

[16] D. L. Fried, “Four-, three-, and two-bin algorithms,” Optical Sciences Company, Anaheim, CA, Tech Rep. TN-187, Dec 2004.

[17] Apogee Imaging Systems, (2010). [Online]. “High performance cooled CCD camera system ALTA U260 data sheet.” www.ccd.com.

[18] T. A. Rhoadarmer and J. D. Barchers, “Noise analysis for complex field estimation using a self-referencing interferometer wave front sensor,” Air Force Research Laboratory, Kirtland Air Force Base, NM, Rep. AFRL-DE-PS-TP-20006-1020, pp. 215–227, 2002.

[19] P. D. Burns, “Signal-to-noise ratio analysis of charge-coupled device imagers,” in *Proceedings of SPIE*, vol. 1242, Santa Clara, CA, 1990, pp. 187–194.

[20] P. Jacquemin, B. Fernandez, C. C. Wilcox, T. Martinez, and B. Agrawal, “Deep horizontal atmospheric turbulence modeling and simulation with a liquid crystal spatial light modulator,” Naval Postgraduate School, Monterey, CA, Tech Rep, 2012.

[21] B. Fernandez, T. Martinez, C. Wilcox, J. J. Kim, and B. N. Agrawal, “Adaptive Optics Testbed for Laboratory Simulation of Deep Atmospheric Turbulence,” presented at the DEPS Beam Control Conference, Monterey, CA, 2013.

[22] D. Dunsby, Y. Gu, and P. M. W. French, “Single-shot phase-stepped wide-field coherence-gated imaging,” *Opt. Express*, vol. 11, pp. 105–115, 2003.

[23] J. Notaras and C. Paterson, “Demonstration of closed-loop adaptive optics with a point-diffraction interferometer in strong scintillation with optical vortices,” *Opt. Express*, vol. 15, pp. 13745–13756, 2007.

INITIAL DISTRIBUTION LIST

1. Defense Technical Information Center
   Ft. Belvoir, Virginia

2. Dudley Knox Library
   Naval Postgraduate School
   Monterey, California